

Response to Reviewer Comments:

We thank the two Anonymous Reviewers for their comments.

Reviewer #1 Comments:

This paper describes results from an observing system simulation experiment (OSSE) to assess the potential to quantify sources of methane from different satellite observing systems. The focus is on emissions at the kilometre scale, both constant in time and transient. The paper is well written, and I recommend publishing after the following minor comments are addressed.

General Comments:

It is amazing to see the enormous improvement in capabilities over the past decades (and in the upcoming decade) to quantify emissions from space with ever increasing spatial (and temporal) resolution. However, one might ask, where the limit would be e.g. in spatial resolution to retrieve useful information e.g. in the context of mitigation. Given the focus on the kilometre scale, and on temporal variations down to hourly, why not go to even smaller scales? I suggest this should be discussed in the introduction to better motivate the targeted spatial and temporal scale.

Excellent question. There were three primary reasons we chose to focus on the kilometer scale:

- 1) **Computational expense.** Computational expense was a major factor in the choice of spatio-temporal resolution; it was a non-trivial endeavor to construct the footprints for this application.
- 2) **Availability of inventories.** To our knowledge, there are not any methane inventories available at sub-kilometer scale that we could use to inform our analysis.
- 3) **Spatial resolution of current and future satellite-based instruments.** The resolution chosen here is finer than the present satellite-based instruments (e.g., GOSAT, TROPOMI, and GeoCARB), so it seemed appropriate for this particular application.

There is ongoing work from a member in the Jacob group examining finer spatial scales than this (50m resolution), however this work is not yet published.

We have added the following text to the introduction:

Lines 66-68: “Our choice of scales is guided by the resolution of the planned satellite observations, and our choice of the Barnett Shale is guided by the availability of a high-resolution emission inventory for the region (Lyon *et al.*, 2015).”

And the following line in Section 2:

Lines 114-116: “Computing these high-resolution footprints was a non-trivial computational task and ultimately yielded more than 4 Tb of footprints for the week of pseudo-satellite observations in the Barnett Shale.”

Specific Comments:

1.) Fig. 4: The methane enhancement looks somewhat patchy, with a number of white pixels with zero or near-zero enhancement next to pixels with significantly larger enhancements. Given that the atmosphere due to advection and mass conservation is expected to be continuous in those enhancements, and given that the grey-scale used for the visualization does not have any step changes, the figure is surprising.

The “patchy-ness” is actually due to a lack of data in a handful of locations. Constructing the footprints at this spatial scale required running 100 trajectories from 12 vertical layers for each column observation. We ultimately constructed more than 300,000 column observations which meant we had in excess of 3.6 million receptor locations for WRF-STILT (each with 100 particles). We included a number of fault tolerances but some of the simulations still crashed (e.g., due to reaching the wall clock for that particular job submission). If any of the 12 vertical layers failed to run successfully then we would have to throw out that column observation.

We have amended the caption to indicate that the patchy-ness is missing data, not zeros.

2.) Fig. 6, right panel: the colour regions don’t follow the lines as they should (and as they do in the left panel).

This actually is correct. In the left panel of Fig. 6 (and 8) we vary the instrument precision and there is a monotonic response. In the right panel of Fig. 6 (and 8) we increase the number of return times and we find that the response is not actually monotonic. Black lines in the panel are the actual eigenvalues for each case and you’ll notice that there are slight overlaps (or crossings) of the black lines. This is because there are a number of ways to change the return time for a satellite.

For example, for the daily observations we use data from 13 local time while the twice daily observations are at 10 and 14 (see Table 1). So the twice daily observations do not include the same observations as the daily observations. This means that the twice daily observations will not necessarily out-perform the daily observations (e.g., if there were more favorable meteorological conditions at 13 local time).

Regarding the shading in Fig. 6 (and 8), we tried a few different ways of presenting the results (e.g., coloring the individual lines) but it was quite messy because a number of the lines are quite close together. This seemed like the best way to present the results.

We have added the following text to the figure caption:

Fig 6 caption: “The change in flux threshold as the sampling frequency increases in the right panel is not necessarily monotonic, this is because some of the cases use different subsets

of observation (e.g., daily observations are at 13 local time while twice daily are at 10 and 14).”

3.) L334-336: Please clarify: you state “Analysis of $\hat{H}\hat{H}^T$ does not yield the eigenvectors of F ”, but the previous sentence states otherwise.

Analysis of $\hat{H}^T\hat{H}$ and $\hat{H}\hat{H}^T$ yield the same eigenvalues but different singular vectors. This can be seen from a singular value decomposition of \hat{H} ($\hat{H} = \mathbf{U}\Sigma\mathbf{V}^T$; where \mathbf{U} and \mathbf{V} are unitary matrices: $\mathbf{I} = \mathbf{U}^T\mathbf{U} = \mathbf{U}\mathbf{U}^T = \mathbf{V}^T\mathbf{V} = \mathbf{V}\mathbf{V}^T$):

$$\begin{aligned}\hat{H}^T\hat{H} &= (\mathbf{U}\Sigma\mathbf{V}^T)^T \mathbf{U}\Sigma\mathbf{V}^T \\ &= \mathbf{V}\Sigma^T\mathbf{U}^T \mathbf{U}\Sigma\mathbf{V}^T \\ &= \mathbf{V}\Sigma^T\Sigma\mathbf{V}^T \\ &= \mathbf{V}\Lambda\mathbf{V}^T\end{aligned}$$

$$\begin{aligned}\hat{H}\hat{H}^T &= \mathbf{U}\Sigma\mathbf{V}^T (\mathbf{U}\Sigma\mathbf{V}^T)^T \\ &= \mathbf{U}\Sigma\mathbf{V}^T \mathbf{V}\Sigma^T\mathbf{U}^T \\ &= \mathbf{U}\Sigma\Sigma^T\mathbf{U}^T \\ &= \mathbf{U}\Lambda\mathbf{U}^T\end{aligned}$$

From this, we can see that analysis of $\hat{H}^T\hat{H}$ and $\hat{H}\hat{H}^T$ would yield the same singular values (Λ), that can be related back to the eigenvalues, but different singular vectors. This means that, depending on the dimension of m and n , we can obtain the eigenvalues by analyzing either $\hat{H}^T\hat{H}$ or $\hat{H}\hat{H}^T$.

We have updated the text in the appendix.

Reviewer #2 Comments:

Turner et al. present an OSSE to assess the performance of different space-based methane measurements (TROPOMI, GeoCarb, aspirational), in particular considering the ability of these different sensors to evaluate methane emissions from the Barnett Shale, a major oil and gas production region in US. This manuscript is very well written – clear, concise, and presents interesting results of particular relevance at this junction in time. I’m supportive of publication once my minor concerns mentioned below are addressed.

General Comments:

1.) Larger context issue: The work as presented lacks some context that limits the extent and value of the conclusions. This could be addressed easily and would make the assessment of what the Barnett shale region looks like as a source region compared to other regions and sources of methane. Is the Barnett a typical oil/gas field (for the US, for the globe)? Are emissions particularly large (or small) from this region? Are emissions particularly spatially heterogeneous (lot of intense point sources? Heavy- tail distribution of emissions?)? How does this compare to other interesting methane source regions? Would

results be extensible to other oil/gas regions? To regions with intense wetlands? The work presented is convincing for the capabilities/limitations of different sensors but I don't know if the 6ppb suggested observational threshold is actually an important threshold for studying any domain other than the Barnett.

Much of the information requested is not available for other regions. To our knowledge, the Barnett Shale is the only oil/gas basin with a high-resolution inventory available (the inventory constructed by the EDF). So it is not easy to compare the distribution of sources to another basin. The availability of a detailed inventory was a major motivator in the choice of the Barnett Shale for this OSSE.

We have added the following text to the introduction:

Lines 68-70: "The pattern and density of methane emissions in the Barnett Shale is typical of other source regions in the US (Maasakkers *et al.*, 2016)."

2.) Question on methodology: What is the impact of choosing to only simulate observations made within the region defined (dashed orange box in Fig. 2)? All the sensors considered would make observation surrounding this box as well, which would have overlapping sensitivity with this region. How does neglecting these observations impact the results? In particular, for sensors like TROPOMI with 'coarser' resolution, might the use of these observation points actually improve the results?

Excellent question. Our present study limited the observation domain to the dashed orange box due to computational expense. Constructing the footprints at the fine spatial scales here required running 100 trajectories from 12 vertical layers for each column observation. We ultimately constructed more than 300,000 column observations, which meant we had in excess of 3.6 million receptor locations for WRF-STILT (each with 100 particles). The library of footprints for this dashed orange box is more than 4 Tb.

However, my previous work has addressed what amounts to effectively the same question just phrased slightly different: "what is the impact of limiting the domain". This previous work (Turner *et al.*, 2016; Supplemental Section 6.1) analyzed the impact of domain size on the error reduction for WRF-STILT inversions in California's Bay Area. We found that it made little difference in that application. That study used "error reduction" as the metric and found roughly 1% less error reduction when using the reduced domain, compared to the base case.

Further, the total weekly footprint (bottom right panel of Fig. 2) shows that footprints are strongly sensitive to the core 70x70 km² region.

We have added the following text:

Lines 121-129: "Additional observations within the outer domain would need to be considered to constrain emissions in that domain. On the other hand, information on emissions in the 70x70 km² core domain is mainly contributed by observations within the domain. Thus our focus will be to determine the capability of the observations in the 70x70 km² domain to constrain emissions within that same domain, but we include the outer

290x235 km² domain in our footprint analysis for completeness in accounting of information. Previous work from Turner et al. (2016; Supplemental Section 6.1) investigated the impact of domain size on error reduction for WRF-STILT inversions in California's Bay Area and found that it had a negligible impact."

Minor Comments:

1.) Line 9: I don't typically think of the Barnett Shale as being in Northeast Texas – it appears more central than anything else.

We have updated the text to refer to it as "Barnett Shale region in Texas".

2.) Line 16: I'm not clear on the statement that TROPOMI is "very limited" on finer spatial scales. Does this mean TROPOMI can resolve one flux value for a 100km pixel and finer is not possible? Or is there some actual finer spatial threshold?

3.) Line 17: 4-37% of total information. It is not clear what this means on reading the abstract at first, and even with the details later in the paper, it would be good to have further clarification on what this percentage is reported as relative to (what is "total information") in this sentence. This relates to clarifying what the 100 pieces of information is.

4.) Line 20: Please be more specific here for the importance of 6ppb. My impression is there is an inflection point in performance at 6ppb where the resolved flux improves drastically.

5.) Line 24: vague – please be more specific.

We have amended the abstract in response to points 2-5.

Lines 15-16: "We find that a week of TROPOMI observations should provide information on temporally invariant emissions at ~30 km spatial resolution."

Lines 16-18: "GeoCARB should provide information available on temporally invariant emissions ~2-7 km spatial resolution depending on sampling frequency (hourly to daily)."

Lines 19-20: "A precision better than 6 ppb is critical for GeoCARB to achieve fine resolution of emissions."

Further discussion of these points was also added to the results section (see tracked changes on Pages 11-12).

6.) Line 51: Important to state the GHGs performance is claimed but not proven.

We no longer mention GHGSat as it is not really relevant to the discussion here.

Assessing the capability of different satellite observing configurations to resolve the distribution of methane emissions at kilometer scales

Alexander J. Turner^{1,2}, Daniel J. Jacob², Joshua Benmergui², Jeremy Brandman³, Laurent White³, and Cynthia A. Randles³

¹College of Chemistry/Department of Earth and Planetary Sciences, University of California, Berkeley, CA, USA.

²School of Engineering and Applied Sciences, Harvard University, Cambridge, Massachusetts, USA.

³ExxonMobil Research and Engineering Company, Annandale, NJ, USA.

Correspondence to: Alexander J. Turner
(alexjturner@berkeley.edu)

Abstract. Anthropogenic methane emissions originate from a large number of fine-scale and of-
ten transient point sources. Satellite observations of atmospheric methane columns are an attrac-
tive approach for monitoring these emissions but have limitations from instrument precision, pixel
resolution, and measurement frequency. Dense observations will soon be available in both low
Earth and geostationary orbits, but the extent to which they can provide fine-scale information on
methane sources has yet to be explored. Here we present an observation system simulation ex-
periment (OSSE) to assess the capabilities of different satellite observing system configurations.
We conduct a 1-week WRF-STILT simulation to generate methane column footprints at 1.3×1.3
 km^2 spatial resolution and hourly temporal resolution over a $290 \times 235 \text{ km}^2$ domain in the Barnett
Shale in Northeast Texas, a major oil/gas field in Texas with a large number of point sources. We sub-
sample these footprints to match the observing characteristics of the recently launched TROPOMI
instrument ($7 \times 7 \text{ km}^2$ pixels, 11 ppb precision, daily frequency), the planned GeoCARB instrument
($2.7 \times 3.0 \text{ km}^2$ pixels, 4 ppb precision, nominal twice-daily frequency), and other proposed observ-
ing configurations. The information content of the various observing systems is evaluated using
the Fisher information matrix and its eigenvalues. We find that a week of TROPOMI observations
should effectively provide regional ($\sim 100 \text{ km}$) provide information on temporally invariant emis-
sions but is very limited at finer scales at $\sim 30 \text{ km}$ spatial resolution. GeoCARB should provide
4-37% of the total information available for information available on temporally invariant emissions
in the Barnett Shale (~ 100 pieces of information 2-7 km spatial resolution depending on sampling
frequency (hourly to daily)). Improvements to the instrument precision yield greater increases in in-

formation content ~~,-compared-to-than~~ improved sampling frequency. A precision better than 6 ppb is ~~an important threshold for achieving critical for GeoCARB to achieve~~ fine resolution of emissions. Transient emissions would be missed with either TROPOMI or GeoCARB. An aspirational high-resolution geostationary instrument with $1.3 \times 1.3 \text{ km}^2$ pixel resolution, hourly return time, and 1 ppb precision would effectively constrain the temporally invariant emissions in the Barnett Shale at the kilometer scale and provide some information on ~~transient-hourly variability of~~ sources.

1 Introduction

Methane is a greenhouse gas emitted by a range of natural and anthropogenic sources (Kirschke et al., 2013; Saunio et al., 2016; Turner et al., 2017). Anthropogenic methane emissions are difficult to quantify because they tend to originate from a large number of potentially transient point sources such as livestock operations, oil/gas leaks, landfills, and coal mine ventilation. Atmospheric methane observations from surface and aircraft have been used to quantify emissions (e.g., Miller et al., 2013; Caulton et al., 2014; Karion et al., 2013, 2015; Lavoie et al., 2015; Conley et al., 2016; Peischl et al., 2015, 2016; Houweling et al., 2016) but are limited in spatial and temporal coverage. Satellite measurements have dense and continuous coverage but limitations from observational errors and pixel resolution need to be understood. Here we perform an observing system simulation experiment (OSSE) to investigate the information content of different configurations of satellite instruments for observing fine-scale and transient methane sources, taking as a test case the oil/gas production sector.

Low-Earth orbit satellite observations of methane by solar backscatter in the shortwave infrared (SWIR) have been available since 2003 from the SCIAMACHY instrument (2003–2012; Frankenberg et al., 2005) and from the GOSAT instrument (2009–present; Kuze et al., 2009, 2016). SWIR instruments measure the atmospheric column of methane with near-unit sensitivity throughout the troposphere. SCIAMACHY and GOSAT demonstrated the capability for high-precision ($<1\%$) measurements of methane from space (Buchwitz et al., 2015), but SCIAMACHY had coarse pixels ($30 \times 60 \text{ km}^2$ in nadir) and GOSAT has sparse coverage (10-km diameter pixels separated by 250 km). Inverse analyses have used observations from these satellite-based instruments to estimate methane emissions at $\sim 100\text{--}1000 \text{ km}$ spatial resolution (e.g., Bergamaschi et al., 2009, 2013; Fraser et al., 2013; Monteil et al., 2013; Wecht et al., 2014a; Cressot et al., 2014; Kort et al., 2014; Turner et al., 2015, 2016a; Alexe et al., 2015; Tan et al., 2016; Buchwitz et al., 2017; Sheng et al., 2018b,a). But such coarse resolution makes it difficult to resolve individual source types because of spatial overlap (Maasakkers et al., 2016).

Improved observations of methane from space are expected in the near future (Jacob et al., 2016).

The ~~GHGSat instrument launched in June 2016 () has $50 \times 50 \text{ m}^2$ effective pixel resolution over selected $12 \times 12 \text{ km}^2$ viewing scenes with a return time of a few weeks, suitable for detecting large point sources. The~~ TROPOMI instrument (Veefkind et al., 2012; Butz et al., 2012; Hu et al., 2016) (Veefkind et al., 2012; Butz et al.,

launched in October 2017, will provide global mapping at 7×7 km² nadir resolution once per day. The GeoCARB geostationary instrument (Polonsky et al., 2014; O’Brien et al., 2016) will be launched in the early 2020s with current design values of 3×3 km² pixel resolution and twice-daily return time. Additional instruments are presently in the proposal stage with improved combinations of pixel resolution, return time, and instrument precision (Fishman et al., 2012; Butz et al., 2015; Xi et al., 2015).

An OSSE simulates the atmosphere as it would be observed by an instrument with a given observing configuration and error specification. Several OSSEs have been conducted to evaluate the potential of satellite observations to quantify methane sources, but they have either been conducted at coarse ($\sim 50\times 50$ km²) spatial resolution (Wecht et al., 2014b; Bousserez et al., 2016) or assumed idealized flow conditions (Bovensmann et al., 2010; Rayner et al., 2014). ~~Jacob et al. (2016) presented a simple mass balance equation to compare the source detection capabilities of satellite instruments with different pixel resolutions, precisions, and return times, but they used information from the source pixel only and assumed a homogeneous flow.~~ Here we use a 1-week simulation of atmospheric methane with 1.3×1.3 km² resolution over a 290×235 km² domain to simulate continuous and transient emissions in the Barnett Shale region of ~~Northeast~~-Texas, and from there we quantify the capability of different satellite instrument configurations to resolve and quantify these sources at the kilometer ~~scale.~~ and hourly scales. Our choice of scales is guided by the resolution of the planned satellite observations, and our choice of the Barnett Shale is guided by the availability of a high-resolution emission inventory for the region (Lyon et al., 2015). The pattern and density of methane emissions in the Barnett Shale is typical of other source regions in the US (Maasakkers et al., 2016).

2 High-resolution OSSE environment

We simulate atmospheric methane concentrations over the Barnett Shale ~~of Northeast~~-in Texas at 1.3×1.3 km² horizontal resolution for the period of October 19-25, 2013 using a framework similar to that of Turner et al. (2016b). The simulation uses version 3.5 of the Weather Research and Forecasting (WRF) model (Skamarock et al., 2008) over a succession of nested domains (left panel in Figure 1) with 1.3×1.3 km² spatial resolution in the innermost domain covering 290×235 km². There are 50 vertical layers up to 100 hPa. Boundary-layer physics are represented with the Mellor-Yamada-Janic scheme and the land surface is represented with the 5-layer slab model (Skamarock et al., 2008). The simulation is initialized with assimilated meteorological observations from the North American Regional Reanalysis (<https://www.ncdc.noaa.gov/data-access/model-data/model-datasets/north-american-regional-reanalysis-narr>). Overlapping 30-hour forecasts were initialized every 24 hours at 00 UTC and the first 6 hours of each forecast were discarded to allow for model spinup. Grid nudging was used in the outer-most domain.

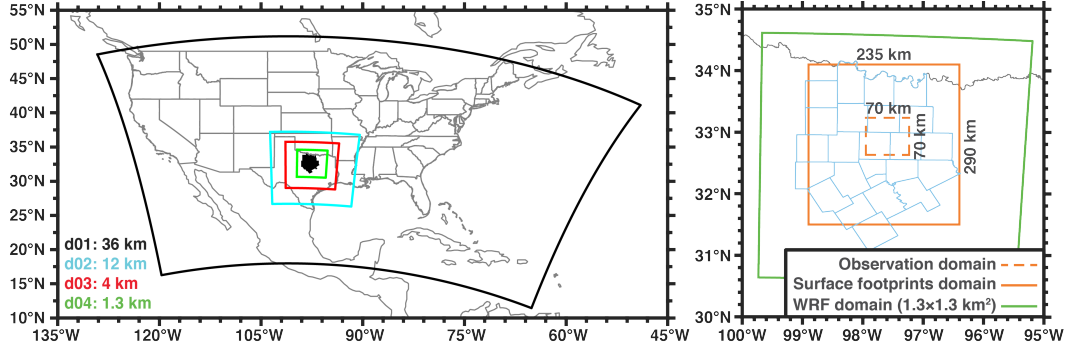


Fig. 1. High-resolution OSSE domain. Left panel shows the successive nested WRF domains at 36, 12, 4, and 1.3 km spatial resolutions, with the coarser domains providing initial and boundary conditions for the finer domains. Black shaded region is the Barnett Shale region of Northeast in Texas. Right panel shows the domain for the OSSE. Green box is the innermost 1.3 km WRF domain, dashed orange box is the observation domain, solid orange box is the domain over which the footprints are computed. Light blue lines indicate the counties in the Barnett Shale.

91 WRF meteorology is used to drive the Stochastic Time-Inverted Lagrangian Transport (STILT)
 92 model (Lin et al., 2003). STILT is a Lagrangian particle dispersion model. It advects an ensemble
 93 of particles backward in time from selected receptor locations, using the archived hourly WRF wind
 94 fields and boundary-layer heights. STILT calculates the footprint for the receptors; a spatio-temporal
 95 map of the sensitivity of observations to emissions contributing to the concentration at each selected
 96 receptor location and time. We use STILT to calculate 10-day footprints for hourly column concen-
 97 trations at $1.3 \times 1.3 \text{ km}^2$ resolution over a $70 \times 70 \text{ km}^2$ domain in the innermost WRF nest, tracking
 98 the resulting footprints over a $290 \times 235 \text{ km}^2$ domain (right panel in Figure 1). With this system we
 99 examine the constraints on emissions over the $290 \times 235 \text{ km}^2$ domain provided by dense SWIR satel-
 100 lite observations (over the $70 \times 70 \text{ km}^2$ domain) that have up to 1.3 km pixel resolution and hourly
 101 daytime frequency. Footprints for each column are obtained by releasing 100 STILT particles from
 102 vertical levels centered at 28 m above the surface, 97 m, 190 m, 300 m, and 8 additional levels up
 103 to 14 km altitude spaced evenly on a pressure grid. The column footprints are then constructed by
 104 summing the pressure-weighted contributions from individual levels, using a typical SWIR averag-
 105 ing kernel taken from Worden et al. (2015) with near-uniformity in the troposphere, and correcting
 106 for water vapor (see Appendix A in O'Dell et al., 2012).

107 The footprint for the i^{th} receptor location and time can be expressed as a vector $\mathbf{h}_i = (\partial y_i / \partial \mathbf{x})^T$
 108 describing the sensitivity of the column concentration y at that receptor location and time to the
 109 emission fluxes \mathbf{x} over the $290 \times 235 \text{ km}^2$ domain and previous times extending up to 10 days. Here
 110 \mathbf{x} is arranged as a vector of length n assembling all the emission grid cells and hours, allowing the
 111 emissions to vary on an hourly basis. The column concentration is expressed as the dry air column-
 112 average mixing ratio (ppb) following common practice (Jacob et al., 2016). The emissions \mathbf{x} have

113 units of $\text{nmol m}^{-2} \text{s}^{-1}$, so that the footprint has units of $\text{ppb nmol}^{-1} \text{m}^2 \text{s}$. The column concentration
 114 for the i^{th} observation (y_i) can be reconstructed from its footprint as:

$$y_i = \mathbf{h}_i \mathbf{x} + b_i \quad (1)$$

115 where b_i is the background column concentration upwind of the $290 \times 235 \text{ km}^2$ domain. We can
 116 then write the full set of observations as a vector \mathbf{y} of length m , and reshape the set of m footprint
 117 vectors \mathbf{h} into an $m \times n$ sparse matrix $\mathbf{H} = \partial \mathbf{y} / \partial \mathbf{x}$ (where m is the number of observations and n is
 118 the number of state vector elements):

$$\mathbf{y} = \mathbf{H} \mathbf{x} + \mathbf{b} \quad (2)$$

119 where \mathbf{b} is the background vector with elements b_i and \mathbf{H} is the Jacobian matrix that maps emissions
 120 to concentration enhancements due to emissions within our domain.

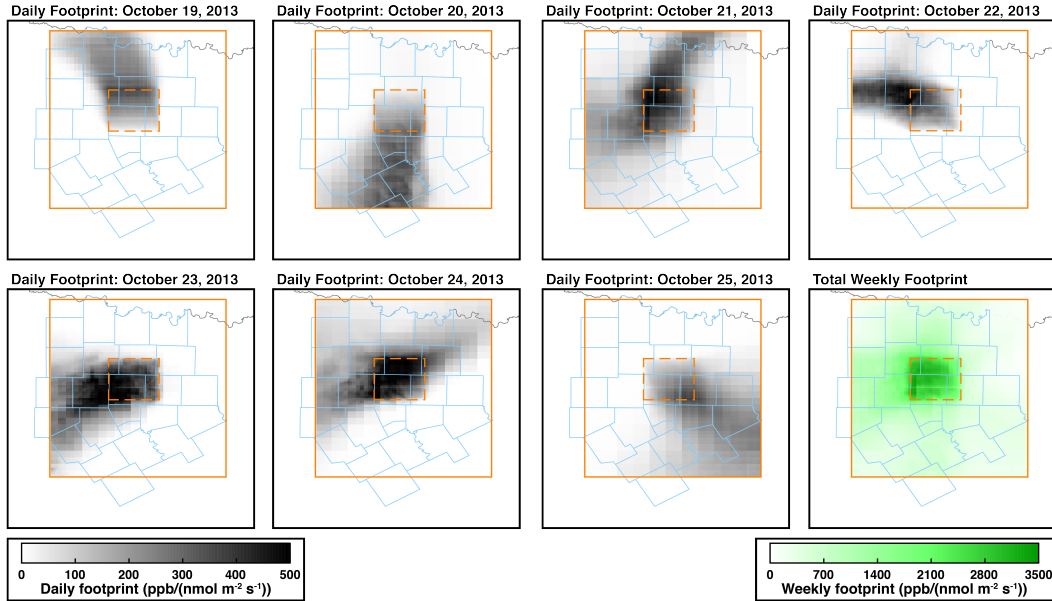


Fig. 2. Summed methane column footprints for all $1.3 \times 1.3 \text{ km}^2$ grid cells in the $70 \times 70 \text{ km}^2$ observation domain defined by the dashed orange box. The footprints are calculated from 8 to 17 local time over the $290 \times 235 \text{ km}^2$ domain defined by the solid orange box. Bottom right panel shows the summed footprint for the full week, ~~sealed by 1/7~~.

121 Figure 2 shows the sum of all column footprints produced on individual days for the $70 \times 70 \text{ km}^2$
 122 observation domain. Computing these high-resolution footprints was a non-trivial computational
 123 task and ultimately yielded more than 4 Tb of footprints for the week of pseudo-satellite observations
 124 in the Barnett Shale. The footprints show large variability from day to day over the course of the
 125 week, reflecting meteorological variability. For example, winds are from the north on October 19th

126 and from the south on October 20th. The winds are weak on October 24th, resulting in a strong local
 127 contribution to the footprint. Summing the footprints over the course of the week (bottom right panel
 128 of Fig. 2), we find that the observations are **strongly-mainly** sensitive to the core $70 \times 70 \text{ km}^2$ domain
 129 where they are made, with a diffuse sensitivity over the outer $290 \times 235 \text{ km}^2$ domain. Additional
 130 observations within the outer domain would need to be considered to constrain emissions in that
 131 domain. On the other hand, information on emissions in the $70 \times 70 \text{ km}^2$ core domain is mainly
 132 contributed by observations within the domain. Thus our focus will be to determine the capability of
 133 the observations in the $70 \times 70 \text{ km}^2$ domain to constrain emissions within that same domain, but we
 134 include the outer $290 \times 235 \text{ km}^2$ domain in our footprint analysis for completeness in accounting of
 135 information. Previous work from (Turner et al., 2016b, Supplemental Section 6.1) investigated the
 136 impact of domain size on error reduction for WRF-STILT inversions in California's Bay Area and
 137 found that it had a negligible impact

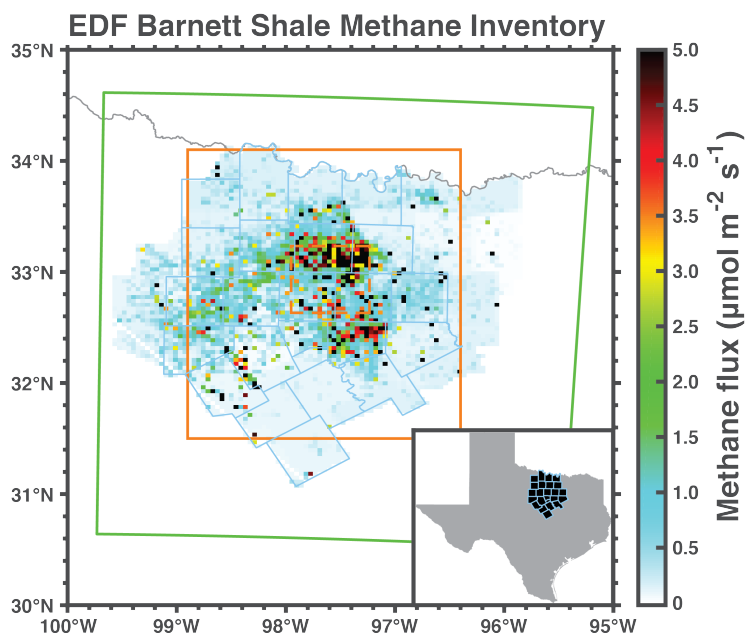


Fig. 3. Gridded Environmental Defense Fund (EDF) methane emission inventory for the Barnett Shale in **Northeast**-Texas in October 2013 (Lyon et al., 2015). Spatial resolution is $4 \times 4 \text{ km}^2$. White areas are outside the inventory domain.

138 The footprint information can be combined with an emission inventory for the $290 \times 235 \text{ km}^2$
 139 domain to generate a field of column concentrations over the $70 \times 70 \text{ km}^2$ domain as would be ob-
 140 served from satellite. We use for this purpose the Environmental Defense Fund (EDF) inventory for
 141 the Barnett Shale in October 2013 at $4 \times 4 \text{ km}^2$ resolution compiled by Lyon et al. (2015). We down-
 142 scale the EDF inventory by uniform attribution from $4 \times 4 \text{ km}^2$ to $1.3 \times 1.3 \text{ km}^2$ spatial resolution.
 143 The inventory is shown in Fig. 3 and includes contributions from oil/gas production, livestock op-

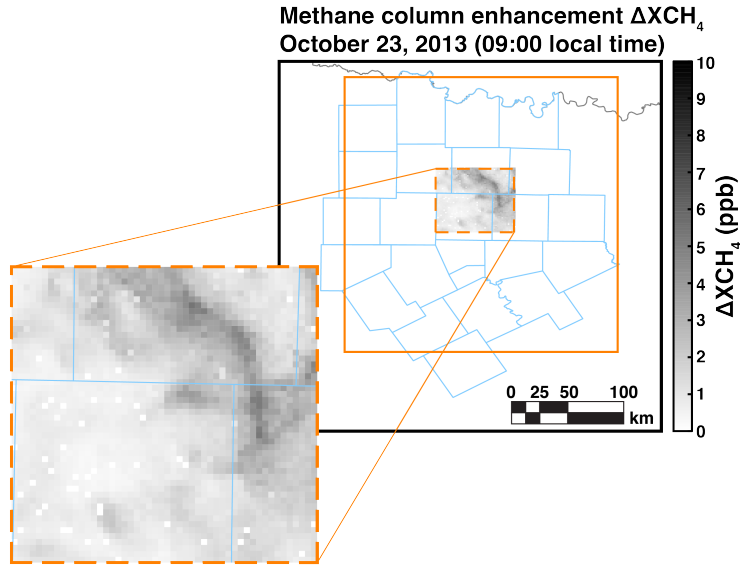


Fig. 4. Simulated methane concentration enhancements relative to background ($\Delta XCH_4 = Hx$) in the 70×70 km² observation domain of the Barnett Shale (dashed orange box), as derived from the downscaled EDF methane inventory (x) and the WRF-STILT footprints (H) within the 290×235 km² OSSE domain (solid orange box). Values are for October 23 at 9 local time. [Zeros are due to missing data because of unfinished computations.](#)

erations, landfills, and urban emissions from the Dallas-Fort Worth area. It provides mean monthly values with no temporal resolution, but presumes that some sources will behave as sporadic large transients (Zavala-Araiza et al., 2015). Figure 4 shows an example of the methane column enhancements above background (Hx) computed at 9 local time on October 23. We find enhancements in the range of 0-10 ppb due to emissions within the 290×235 km² OSSE footprint domain. In what follows we will examine the potential of different satellite observing systems to detect these enhancements relative to the background and interpret them in terms of local sources.

3 Information content of different satellite observing systems

We aim to determine the information content from different satellite-based observing systems regarding the spatial and temporal distribution of emissions in the Barnett Shale. We consider both steady and potentially transient emissions with 5 different satellite observing configurations (Table 1). TROPOMI (global daily mapping, 7×7 km² nadir pixel resolution, 11 ppb precision; Veefkind et al., 2012) was launched in October 2017 and is expected to provide an operational data stream by the end of 2018. GeoCARB (geostationary, 2.7×3.0 km² pixel resolution, 4 ppb precision; O'Brien et al., 2016) is planned for launch in the early 2020s and its observation schedule is still under discussion with a tentative design for observations twice daily; here we examine different return frequencies of

Table 1. Satellite observing systems considered in this work.

Instrument	Observation Frequency ^a	Pixel resolution	Precision
		(km ²)	(ppb)
hi-res ^b	hourly	1.3×1.3	1.0
GeoCARB (hourly)	hourly	2.7×3.0	4.0
GeoCARB	twice daily	2.7×3.0	4.0
GeoCARB (daily)	daily	2.7×3.0	4.0
TROPOMI	daily	7.0×7.0	10.8

^aHourly observations are 10 times per day at 8-17 local time, twice daily observations are at 10 and 14 local time, and daily observations are at 13 local time.

^bAspirational instrument with the highest observation frequency and pixel resolution that can be simulated within our OSSE framework.

hourly, twice daily, and daily. Finally, the hypothetical “hi-res” configuration assumes geostationary hourly observations at the 1.3×1.3 km² pixel resolution of our WRF simulation and with 1 ppb precision; it represents an aspirational system that combines the frequent return time, fine pixel resolution, and high precision of instruments presently at the proposal stage (Bovensmann et al., 2010; Fishman et al., 2012; Xi et al., 2015). All configurations are filtered for cloudy scenes.

The various satellite observing configurations of Table 1 differ in their return frequency, pixel resolution, and instrument precision. The benefit of improving any of these attributes may be limited by error in the forward model used in the inverse analysis (i.e., the Jacobian matrix \mathbf{H}) and by spatial or temporal correlation of the errors. These limitations are described by the model-data mismatch error covariance matrix (\mathbf{R}) including summed contributions from the instrument, forward model, and representation errors (Turner and Jacob, 2015; Brasseur and Jacob, 2017). Representation errors are negligible here because the instrument pixels are commensurate or coarser than the model grid resolution. Instrument error (i.e., precision) is listed in Table 1. Forward model error is estimated by computing STILT footprints for a subset of the meteorological period using the Global Data Assimilation System (GDAS; <https://www.ncdc.noaa.gov/data-access/model-data/model-datasets/global-data-assimilation-system-gdas>), applying the two sets of footprints to either the EDF methane inventory (Fig. 3; Lyon et al., 2015) or the gridded EPA inventory (Maasakkers et al., 2016), and computing semivariograms of differences in column concentrations. From this we obtain a forward model error standard deviation of 4 ppb with an error correlation length scale of 40 km. We assume a temporal model error correlation length of 2 hours. Sheng et al. (2018b) previously derived a temporal model error correlation length of 5 hours in simulation of TCCON methane column observations at 25 km resolution, and we expect our correlation length to be shorter because of the finer resolution.

Bayesian inference is commonly used when estimating methane emissions with atmospheric ob-

184 servations, allowing for errors in the observations and in the prior estimates:

$$P(\mathbf{x}|\mathbf{y}) \propto P(\mathbf{y}|\mathbf{x})P(\mathbf{x}) \quad (3)$$

185 where $P(\mathbf{x}|\mathbf{y})$ is the posterior probability density function (pdf) of the state vector (\mathbf{x}) given the
 186 observations (\mathbf{y}), $P(\mathbf{y}|\mathbf{x})$ is the conditional pdf of \mathbf{y} given \mathbf{x} , and $P(\mathbf{x})$ is the prior pdf of \mathbf{x} . A
 187 common assumption is that $P(\mathbf{y}|\mathbf{x})$ and $P(\mathbf{x})$ are normally distributed which allows us to write the
 188 posterior pdf as

$$P(\mathbf{x}|\mathbf{y}) \propto \exp \left\{ -\frac{1}{2}(\mathbf{y} - \mathbf{H}\mathbf{x})^T \mathbf{R}^{-1}(\mathbf{y} - \mathbf{H}\mathbf{x}) - \frac{1}{2}(\mathbf{x} - \mathbf{x}_a)^T \mathbf{B}^{-1}(\mathbf{x} - \mathbf{x}_a) \right\} \quad (4)$$

189 where \mathbf{B} is the $n \times n$ prior error covariance matrix and \mathbf{x}_a is the $n \times 1$ vector of prior fluxes. The
 190 most probable solution is obtained by minimizing the cost function:

$$\mathcal{J}(\mathbf{x}) = \frac{1}{2}(\mathbf{y} - \mathbf{H}\mathbf{x})^T \mathbf{R}^{-1}(\mathbf{y} - \mathbf{H}\mathbf{x}) + \frac{1}{2}(\mathbf{x} - \mathbf{x}_a)^T \mathbf{B}^{-1}(\mathbf{x} - \mathbf{x}_a) \quad (5)$$

191 yielding the posterior estimate ($\hat{\mathbf{x}}$):

$$\hat{\mathbf{x}} = \mathbf{x}_a + \underbrace{(\mathbf{H}^T \mathbf{R}^{-1} \mathbf{H} + \mathbf{B}^{-1})^{-1}}_{\text{posterior covariance matrix}} \mathbf{H}^T \mathbf{R}^{-1}(\mathbf{y} - \mathbf{H}\mathbf{x}_a) \quad (6)$$

192 with an $n \times n$ posterior error covariance matrix:

$$\mathbf{Q} = \underbrace{(\mathbf{H}^T \mathbf{R}^{-1} \mathbf{H})}_{\text{observations}} + \underbrace{\mathbf{B}^{-1}}_{\text{prior}} \quad (7)$$

193 that characterizes the uncertainty in the solution. The first term in the posterior covariance ma-
 194 trix is known as the Fisher information matrix: $\mathcal{F} = \mathbf{H}^T \mathbf{R}^{-1} \mathbf{H}$ (see, for example, Rodgers, 2000;
 195 Tarantola, 2004). \mathcal{F} defines the observational contribution to the posterior uncertainty.

196 Comparison between \mathcal{F} and \mathbf{B}^{-1} identifies the extent to which the observations reduce the un-
 197 certainty in the fluxes. Specifically, the number of pieces of information on emissions acquired to
 198 better than measurement error is the number of eigenvalues of $\mathbf{B}^{1/2} \mathcal{F} \mathbf{B}^{1/2}$ that are greater than
 199 unity (Rodgers, 2000). As such, the Fisher information matrix and prior error covariance matrix can
 200 quantify the effective rank of the observing system.

201 A drawback with this formulation of the information content is that it relies on the assumption of
 202 a Gaussian prior pdf. A number of papers have suggested that the pdf of methane emissions from a
 203 given source may be skewed, with a “fat tail” of transient high emissions (e.g., Brandt et al., 2014;
 204 Zavala-Araiza et al., 2015; Frankenberg et al., 2016). Alternate formulations for the cost function
 205 to be minimized may include no prior information (least-squares regression), a prior constraint that
 206 promotes a sparse solution (e.g., Candes and Wakin, 2008), a prior constraint based on frequen-
 207 tist regularization approaches (such as LASSO regression or Tikhonov regularization), or a prior

Table 2. Cost functions for different formulations of the inverse problem^a.

Method	Cost function
Least-squares regression	$(\mathbf{y} - \mathbf{H}\mathbf{x})^T \mathbf{R}^{-1} (\mathbf{y} - \mathbf{H}\mathbf{x})$
LASSO regression	$(\mathbf{y} - \mathbf{H}\mathbf{x})^T \mathbf{R}^{-1} (\mathbf{y} - \mathbf{H}\mathbf{x}) + \gamma \sum_i x_i $
Tikhonov regularization	$(\mathbf{y} - \mathbf{H}\mathbf{x})^T \mathbf{R}^{-1} (\mathbf{y} - \mathbf{H}\mathbf{x}) + \gamma \mathbf{x}^T \mathbf{x}$
Bayesian inference, Gaussian	$(\mathbf{y} - \mathbf{H}\mathbf{x})^T \mathbf{R}^{-1} (\mathbf{y} - \mathbf{H}\mathbf{x}) + (\mathbf{x} - \mathbf{x}_a)^T \mathbf{B}^{-1} (\mathbf{x} - \mathbf{x}_a)$
Geostatistical inverse model	$(\mathbf{y} - \mathbf{H}\mathbf{x})^T \mathbf{R}^{-1} (\mathbf{y} - \mathbf{H}\mathbf{x}) + (\mathbf{x} - \mathbf{G}\boldsymbol{\beta})^T \mathbf{B}^{-1} (\mathbf{x} - \mathbf{G}\boldsymbol{\beta})$

^a γ is the regularization parameter for LASSO regression and Tikhonov regularization. \mathbf{G} is a matrix with columns corresponding to different spatial datasets and $\boldsymbol{\beta}$ is a vector of drift coefficients for the spatial datasets. Other variables defined in the text.

constraint based on the spatial patterns of emissions rather than their magnitudes (geostatistical in-
version). Table 2 lists the corresponding formulations. From Table 2 we see that the observation term
is the same in all cases. Thus the Fisher information matrix provides a general measure of the in-
formation content provided by an observing system, independent of the form of the prior constraint,
and we use it in what follows as a measure of the information content.

The Fisher information matrix is an $n \times n$ matrix. Each of its n eigenvectors represent an inde-
pendent normalized emission flux pattern and the corresponding eigenvalues are the inverses of the
error variances associated with that pattern. A more useful way of stating this is that the inverse
square root of the i^{th} eigenvalue of \mathcal{F} represents the flux threshold f_i needed for the observations
to be able to constrain the emission flux pattern represented by the i^{th} eigenvector. Whether that
flux threshold is useful depends on the magnitude of the emissions, and this can be assessed for the
problem at hand. Thus the eigenanalysis of the Fisher information matrix gives us a general estimate
of the capability of an observing system to quantify emissions, which can then be applied to any
actual $n \times n$ emission field.

For a given emission field, we may expect that some of the n emission flux patterns will be
usefully constrained by the observing system while others are not. The number of patterns that are
usefully constrained represents the number $\mathcal{I} \leq n$ pieces of information on emissions provided by
the observing system. We will equivalently refer to it as the rank of the Fisher information matrix.
This is determined by comparing the eigenvalues of an emission inventory (e_i) to the flux thresholds.
The number of e_i larger than the corresponding f_i provides a cut-off to estimate \mathcal{I} :

$$\mathcal{I} = \sum_i \begin{cases} 1, & e_i > f_i \\ 0, & e_i \leq f_i \end{cases} \quad (8)$$

In the case of Bayesian inference, this is roughly equivalent to the degrees of freedom for signal with
a diagonal prior error covariance matrix and a relative uncertainty of 100%. But the eigenanalysis
of the Fisher information matrix provides a more general approach of the capability of an observ-
ing system that can be confronted to any prior constraint and allows intercomparison of different

232 observing system configurations.

233 There is an inconsistency in this formulation of \mathcal{I} : \mathcal{F} and \mathbf{B}^{-1} have different eigenspaces. In this
234 work we have chosen to treat these matrices separately because, in practice, it is computationally
235 infeasible to directly compute the eigenvalues of the matrix product if n is large, as in the case here
236 of constraining hourly emissions of the spatially distributed inventory. This inconsistency results in
237 our estimate of \mathcal{I} likely being an upper bound on the information content (see Appendix for details).

238 4 Comparing different satellite configurations

239 The eigenanalysis of Section 3 allows us to intercompare the value of different satellite configura-
240 tions for resolving the fine-scale patterns of methane emissions within a given domain. Here we
241 apply it to the Barnett Shale domain of Section 2. We consider two limiting cases: Case #1 assumes
242 the emissions to be temporally invariant and Case #2 assumes the emissions to vary hourly with no
243 temporal correlation. In Case #1 the problem is typically overdetermined ($m > n$), depending on
244 the satellite configuration, and the maximum rank of \mathcal{F} is n (the number of emission grid cells). In
245 Case #2 the problem is underdetermined ($m < n$) and the maximum rank of \mathcal{F} is m (the number of
246 observations).

247 In both Case #1 and #2, the observations only provide useful information (as defined by Eq. 8) if
248 the signal is larger than the noise, as diagnosed by the $e_i > f_i$ criterion of Eq. 8. Here the emissions
249 are the downscaled EDF inventory, which includes 40,140 grid cells in the 290×235 km² inversion
250 domain ($n = 40,140$ in Case #1 with temporally invariant emissions) but only 2,601 of those grid
251 cells are within the 70×70 km² observation domain (dashed orange box in Fig. 1) where we might
252 expect the observations to provide the strongest constraints. In Case #2 with temporally variable
253 emissions we have $n = 40,140 \times 24 = 963,360$ grid cells for a single day.

254 Figure 5 shows the ensemble of flux thresholds for the five satellite configurations, assuming
255 temporally invariant emissions. The ranked flux patterns are on the abscissa; leading flux patterns
256 correspond to larger patterns of variability (e.g., regional-scale emissions), and the trailing flux pat-
257 terns correspond to fine-scale variability. The corresponding flux thresholds are on the ordinate.
258 The flux threshold is lowest for the leading flux patterns and largest for the trailing flux patterns.
259 This means that the regional-scale emissions are easiest to quantify and the finer-scale emissions are
260 increasingly difficult to quantify. The information content (\mathcal{I}) is obtained from the intersection of
261 the flux thresholds (colored lines) with the eigenvalues from the emission inventory (black line). A
262 higher information content means that finer scales of emission variability can be detected.

263 From Fig. 5, we see that a week of TROPOMI observations provides 5 pieces of information ;
264 ~~indicating that TROPOMI should be able to constrain the mean emissions from the Barnett Shale~~
265 ~~and the coarse spatial distribution of these emissions ; on emissions for the 70×70 km² core domain~~
266 ~~out of a possible 2601 pieces of information describing the emissions on the 1.3×1.3 km² grid.~~

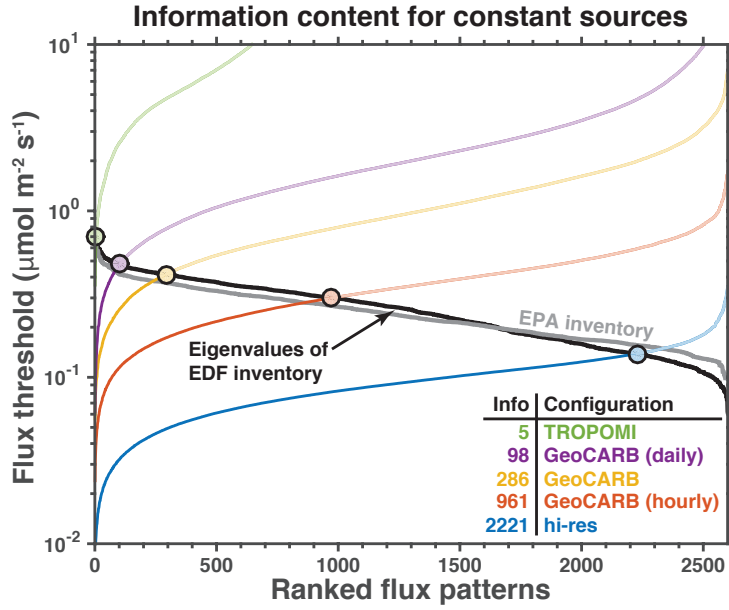


Fig. 5. Capability of different configurations for satellite observations of atmospheric methane (Table 1) to resolve the fine-scale ($1.3 \times 1.3 \text{ km}^2$) patterns of variability of temporally invariant emissions in a $290 \times 235 \text{ km}^2$ domain and for a 1-week observation period. The colored lines show the flux thresholds for the different emission patterns of variability in the domain, as given by the ordered inverse square roots of the eigenvalues of the Fisher information matrix. Solid black line is the eigenvalues of the emissions from the EDF Barnett Shale methane inventory (Lyon et al., 2015) and the solid gray line is the gridded EPA inventory. The region above the black line is where the noise is larger than the signal. Filled circles indicate the information content of the observing system (I) for a given satellite configuration at $1.3 \times 1.3 \text{ km}^2$ spatial resolution. Inset table lists the information contents for the five configurations.

The actual pieces of information are the eigenvectors of the Fisher information matrix, and the ranked eigenvectors describe gradually finer patterns of variability from 70×70 to $1.3 \times 1.3 \text{ km}^2$. The k^{th} ranked eigenvector may be assumed to describe an emission pattern of dimension $70/\sqrt{k}$, implying that TROPOMI can resolve emissions on a 30 km scale.

The three GeoCARB configurations provide 98–961 pieces of information dependent on whether the observations are daily, twice daily, or hourly. Following the above assumption, this corresponds to resolving emissions on a $\sim 2\text{--}7 \text{ km}$ scale. Hourly observations provide 10 times more information (as defined by Eq. 8) on emission patterns than daily observations, and 3 times more than twice-daily observations (the default configuration of GeoCARB). Remarkably, more is gained by going from daily to twice-daily (factor of 3.4) than going from twice-daily to hourly (factor of 2.9), because of the temporal error correlation in the transport model. The aspirational hi-res satellite configuration provides 2,221 pieces of information on temporally invariant sources, corresponding to 85% of the flux patterns in the $70 \times 70 \text{ km}^2$ observation region, which means that much of the spatial variability

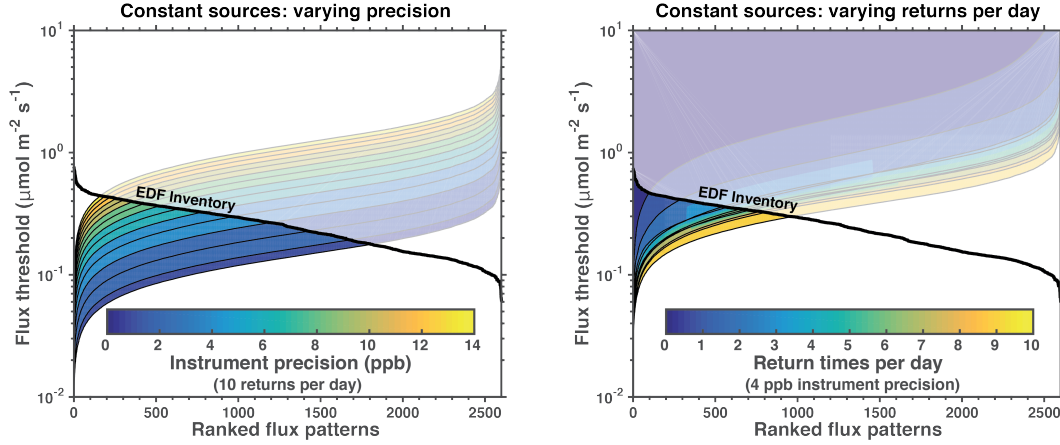


Fig. 6. Capability of GeoCARB-like satellite configurations to resolve the fine-scale ($1.3 \times 1.3 \text{ km}^2$) patterns of variability of temporally invariant emissions in a $290 \times 235 \text{ km}^2$ domain and for a 1-week observation period. Left panel shows the results for a configuration with 10 returns per day (hourly observations) where the instrument precision is varied from 0 to 14 ppb. Right panel shows the results for a configuration with 4 ppb instrument precision and the return frequency per day is varied from 1 to 10. Solid black line shows eigenvalues of the EDF Barnett Shale methane emission inventory (Lyon et al., 2015). The region above the black line is where the noise is larger than the signal. [The change in flux threshold as the sampling frequency increases in the right panel is not necessarily monotonic, this is because some of the cases use different subsets of observation \(e.g., daily observations are at 13 local time while twice daily are at 10 and 14\).](#)

280 in the $1.3 \times 1.3 \text{ km}^2$ emissions in the Barnett Shale is resolved.

281 Figure 6 further quantifies the importance of instrument precision and return frequency for the
 282 GeoCARB pixel resolution of $2.7 \times 3.0 \text{ km}^2$. It shows the flux thresholds for a set of configurations
 283 where the instrument precision is varied from 0 to 14 ppb and the return frequency is varied from 1
 284 to 10 returns per day. We find that instrument precision is more important than return frequency for
 285 increasing the information content from the observations.

286 In Case #2 we assume that the methane sources in individual pixels vary in time on an hourly
 287 basis with no correlation from one hour to the next, making the problem generally underdetermined
 288 ($m < n$) for all satellite configurations. Here we aim to determine the ability of the satellite obser-
 289 vations to quantify the hourly emissions over the spatial patterns defined by the eigenvectors of \mathcal{F}
 290 and making no assumption as to the persistence of those emissions. We treat each day independently
 291 and compute the eigenvalues of the Fisher information matrix for each day. Figure 7 shows the
 292 flux thresholds for the five satellite configurations on a representative day. From Fig. 7, we see that
 293 TROPOMI is unable to provide any information on hourly emissions in the Barnett Shale. The three
 294 GeoCARB configurations provide 2–54 pieces of information. Fig. 8 evaluates the impact of sam-
 295 pling frequency and instrument precision for the GeoCARB configurations. As with the temporally
 296 invariant case, we find that instrument precision is more important for increasing the information

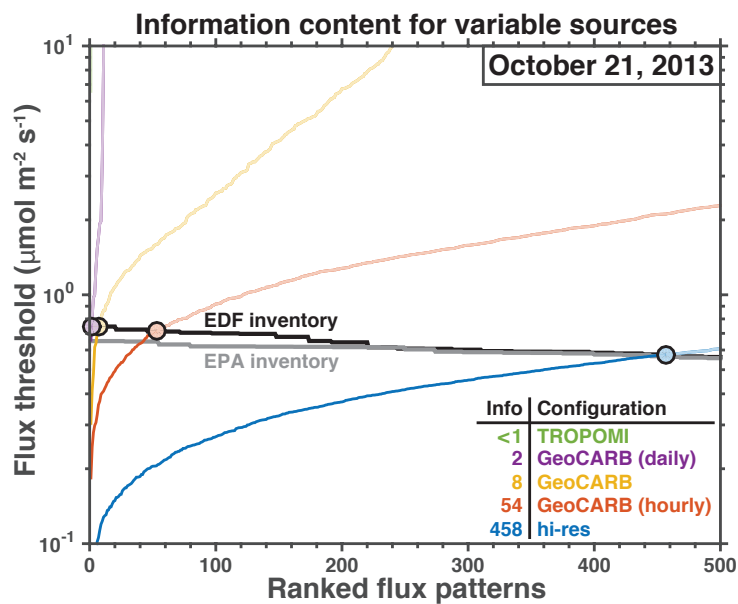


Fig. 7. Same as Fig. 5 but for temporally variable sources on October 21, 2013.

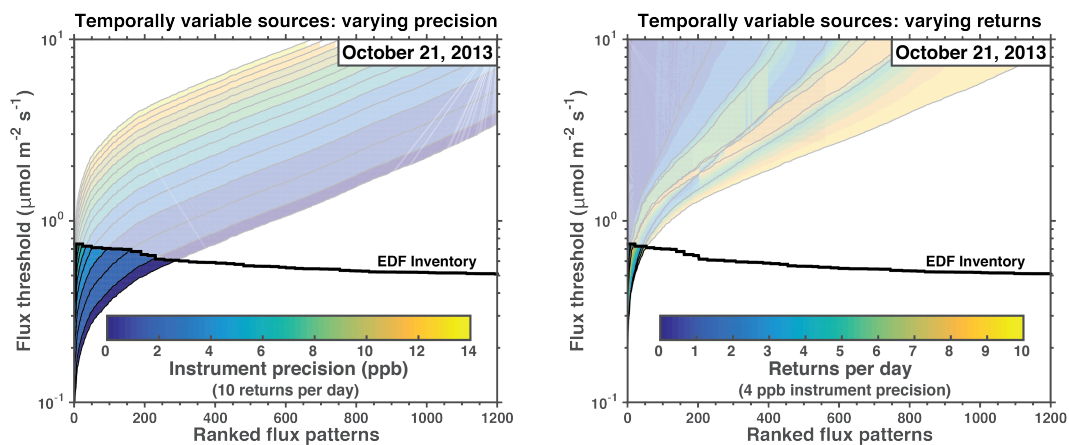


Fig. 8. Same as Fig. 6 but for temporally variable sources on October 21, 2013.

297 content. The aspirational “hi-res” configuration (shown in Fig. 7) is the only configuration that is
 298 able to provide substantial information (458 pieces of information) on temporally variable emissions.

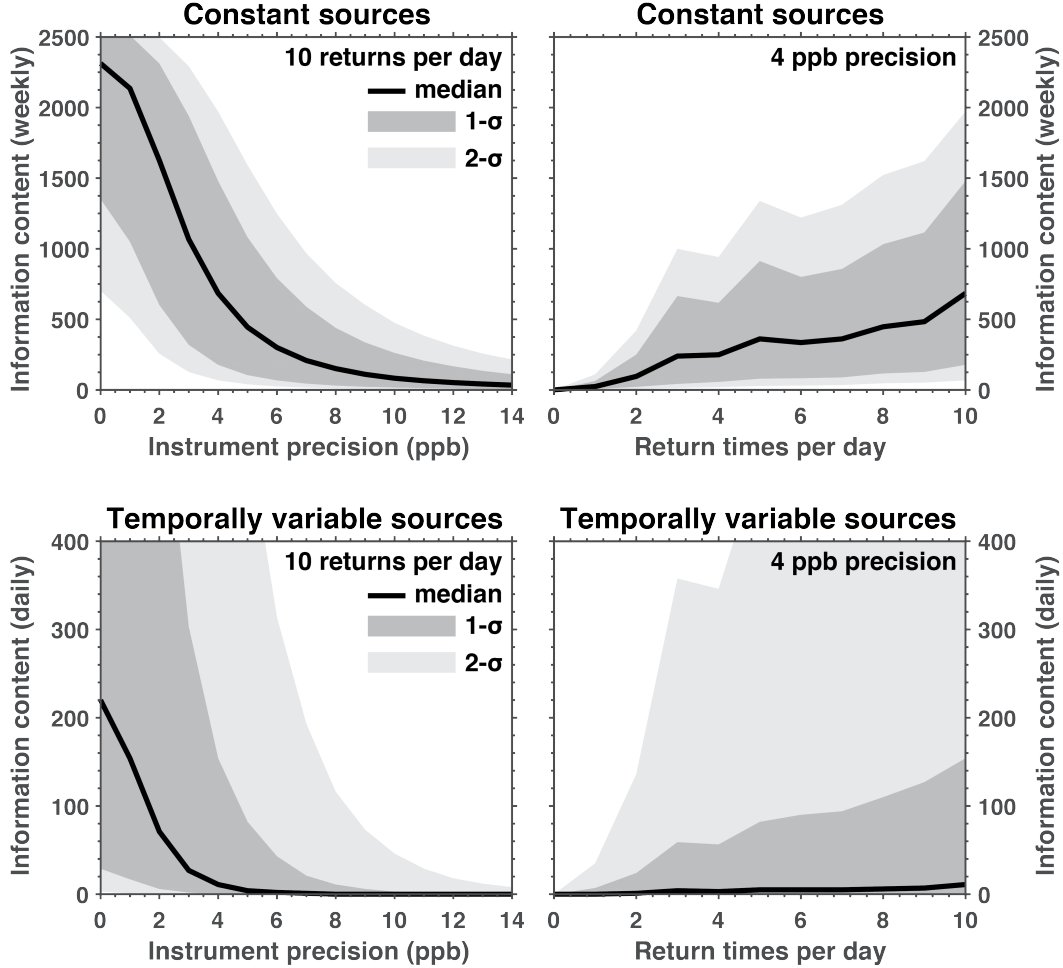


Fig. 9. Information content \mathcal{I} as a function of the instrument precision (left column) and the sampling frequency per day (right column) for a satellite with a pixel resolution of $2.7 \times 3.0 \text{ km}^2$. Top row is for Case #1 where the sources are assumed to be temporally invariant and bottom row is for Case #2 where the sources are temporally variable. Solid black line is the median information content. A 4 ppb model error is included, see Section 3. Uncertainty is from randomly sampling e_i from the eigenvalues of the EDF inventory.

299 Figure 9 summarizes the findings from Figs. 6 and 8. It compares the information content \mathcal{I} from
 300 configurations with $2.7 \times 3.0 \text{ km}^2$ spatial resolution (GeoCARB) as the instrument precision and
 301 return frequency are varied from 0 to 14 ppb and 1 to 10 returns per day, respectively, for both tem-
 302 porally variable and constant sources. Uncertainty on \mathcal{I} is estimated by randomly sampling e_i from
 303 the ensemble of emission inventory eigenvalues and comparing to f_i in Eq. 8. For the temporally
 304 invariant sources (Case #1), we find considerable increases in information content for instrument pre-
 305 cisions better than 6 ppb (top left panel in Fig. 9) and an approximately linear relationship between

information content and return frequency (top right panel in Fig. 9). The satellite configurations provide considerably less information for the temporally variable sources (Case #2). We find that satellite configurations with ~~an instrument precisions~~ instrument precision worse than 6 ppb provide no information on temporally variable sources (bottom left panel in Fig. 9). As with the temporally invariant case, we find an approximately linear relationship between information content and return frequency (bottom right panel in Fig. 9). From this, we conclude that a GeoCARB-like instrument would greatly benefit from having an instrument precision better than 6 ppb.

5 Conclusions

We conducted an observing system simulation experiment (OSSE) to evaluate the potential of different satellite observation systems for atmospheric methane to quantify methane emissions at kilometer scale. This involved a 1-week WRF-STILT simulation of atmospheric methane columns with $1.3 \times 1.3 \text{ km}^2$ spatial resolution over ~~a the~~ 290 \times 235 km^2 domain (Barnett Shale of Northeast Texas) Barnett Shale domain to quantify the information content of different satellite instrument configurations for resolving the kilometer-scale distribution of methane emissions within that domain. We evaluated the information content of the different satellite observing systems through an eigenanalysis of the Fisher information matrix \mathcal{F} , which characterizes the capability of an observing system independently of the form of the prior information. The eigenvalues of \mathcal{F} define the emission flux thresholds for detection of emission patterns down to 1.3 km in scale as defined by the eigenvectors. Here we put these flux thresholds in context of the high-resolution EDF emission inventory for the Barnett Shale to quantify the information content from different satellite observing configurations. The same approach could be readily used for different observation domains and different prior inventories.

We find from this analysis that the recently launched TROPOMI satellite instrument (low Earth orbit, $7 \times 7 \text{ km}^2$ pixels, daily return time, 11 ppb precision) should be able to constrain the mean emissions in the Barnett Shale and provide some coarse-resolution information on the distribution of ~~emissions~~ temporally invariant emissions at $\sim 30 \text{ km}$ scales. The planned GeoCARB instrument (geostationary orbit, $2.7 \times 3.0 \text{ km}^2$ pixels, twice-daily return time, 4 ppb precision), will provide 50 times more information than TROPOMI. The observing frequency of GeoCARB is still under discussion; we find that twice-daily observations triple the information content relative to daily observations, while hourly observations allow another tripling. The 4 ppb precision of GeoCARB is well adapted to the magnitude of methane sources; we find that a precision larger than 6 ppb would considerably decrease the information content. An aspirational “hi-res” instrument using attributes of currently proposed instruments (geostationary orbit, $1.3 \times 1.3 \text{ km}^2$ pixels, hourly return time, 1 ppb precision) can resolve much of the kilometer-scale spatial distribution in the EDF inventory. This assumes that the emissions are constant in time or that their temporal variability is known. Resolv-

ing hourly variable emissions at the kilometer-scale will be very limited even with the aspirational “hi-res” instrument.

Appendix Computing the information content

We treat \mathcal{F} and \mathbf{B}^{-1} separately because it is computationally infeasible to compute the eigenvalues of the matrix product when we attempt to resolve hourly emissions as $n > 10^6$ and both \mathcal{F} and \mathbf{B}^{-1} are $n \times n$ matrices. This separation of \mathcal{F} and \mathbf{B}^{-1} results in our estimate of \mathcal{I} likely being an upper bound on the information content. This follows from Bhatia (1997) who prove that $\lambda(\mathbf{CD}) \prec_w \lambda^\downarrow(\mathbf{C}) \cdot \lambda^\downarrow(\mathbf{D})$, where \mathbf{C} and \mathbf{D} are Hermitian positive definite matrices, $\lambda^\downarrow(\mathbf{X})$ denotes the vector of eigenvalues of \mathbf{X} in decreasing order, \prec_w is the weak majorization preorder, and $\mathbf{p} \cdot \mathbf{q} = (p_1 q_1, \dots, p_n q_n)$. Therefore, directly computing the eigenvalues of $\mathbf{B}^{1/2} \mathcal{F} \mathbf{B}^{1/2}$, as Rodgers (2000) suggests for the Bayesian inference case with Gaussian errors, would likely yield fewer eigenvalues larger than unity than our estimate.

In the case of temporally variable emissions, the system is generally underdetermined ($m < n$) and we can use a singular value decomposition to efficiently compute the eigenvalues of \mathcal{F} . For an $m \times n$ real matrix \mathbf{A} , the non-zero singular values of $\mathbf{A}^T \mathbf{A}$ and $\mathbf{A} \mathbf{A}^T$ are identical even though the singular vectors are different (see, for example, Rodgers, 2000) but the dimensions of these two matrices are $n \times n$ and $m \times m$, respectively, and the eigenvalues can be computed from the square root of the non-zero singular values. We can write $\mathcal{F} = \hat{\mathbf{H}}^T \hat{\mathbf{H}}$ where $\hat{\mathbf{H}} = \mathbf{L}^{-1} \mathbf{H}$ is the pre-whitened Jacobian and \mathbf{L} is a lower triangular matrix from a Cholesky decomposition of \mathbf{R} (such that $\mathbf{R} = \mathbf{L} \mathbf{L}^T$). Thus, the eigenvalues of \mathcal{F} can be obtained by analysis of either $\hat{\mathbf{H}}^T \hat{\mathbf{H}}$ (an $n \times n$ matrix) or $\hat{\mathbf{H}} \hat{\mathbf{H}}^T$ (an $m \times m$ matrix). ~~Analysis of $\hat{\mathbf{H}} \hat{\mathbf{H}}^T$ does not yield the eigenvectors of \mathcal{F} .~~

Acknowledgements. This work was supported by the ExxonMobil Research and Engineering Company and the US Department of Energy (DOE) Advanced Research Projects Agency – Energy (ARPA-E). A. J. Turner is supported as a Miller Fellow with the Miller Institute for Basic Research in Science at UC Berkeley. This research used the Savio computational cluster resource provided by the Berkeley Research Computing program at the University of California, Berkeley (supported by the UC Berkeley Chancellor, Vice Chancellor for Research, and Chief Information Officer). This research also used resources from the National Energy Research Scientific Computing Center, which is supported by the Office of Science of the U.S. Department of Energy under Contract No. DE-AC02-05CH11231. We also acknowledge high-performance computing support from Cheyenne (doi:10.5065/D6RX99HX) provided by NCAR’s Computational and Information Systems Laboratory, sponsored by the National Science Foundation.

372 References

- 373 Alexe, M., Bergamaschi, P., Segers, A., Detmers, R., Butz, A., Hasekamp, O., Guerlet, S., Parker, R., Boesch,
374 H., Frankenberg, C., Scheepmaker, R. A., Dlugokencky, E., Sweeney, C., Wofsy, S. C., and Kort, E. A.:
375 Inverse modelling of CH₄ emissions for 2010–2011 using different satellite retrieval products from GOSAT
376 and SCIAMACHY, *Atmospheric Chemistry and Physics*, 15, 113–133, doi:10.5194/acp-15-113-2015, 2015.
- 377 Bergamaschi, P., Frankenberg, C., Meirink, J. F., Krol, M., Villani, M. G., Houweling, S., Dentener, F., Dlu-
378 gokencky, E. J., Miller, J. B., Gatti, L. V., Engel, A., and Levin, I.: Inverse modeling of global and re-
379 gional CH₄ emissions using SCIAMACHY satellite retrievals, *Journal of Geophysical Research*, 114, doi:
380 10.1029/2009jd012287, 2009.
- 381 Bergamaschi, P., Houweling, S., Segers, A., Krol, M., Frankenberg, C., Scheepmaker, R. A., Dlugokencky, E.,
382 Wofsy, S. C., Kort, E. A., Sweeney, C., Schuck, T., Brenninkmeijer, C., Chen, H., Beck, V., and Gerbig, C.:
383 Atmospheric CH₄ in the first decade of the 21st century: Inverse modeling analysis using SCIAMACHY
384 satellite retrievals and NOAA surface measurements, *Journal of Geophysical Research: Atmospheres*, 118,
385 7350–7369, doi:10.1002/jgrd.50480, 2013.
- 386 Bhatia, R.: *Matrix Analysis*, Graduate Texts in Mathematics, Springer, New York, 1997.
- 387 Bousserez, N., Henze, D. K., Rooney, B., Perkins, A., Wecht, K. J., Turner, A. J., Natraj, V., and Worden,
388 J. R.: Constraints on methane emissions in North America from future geostationary remote-sensing mea-
389 surements, *Atmospheric Chemistry and Physics*, 16, 6175–6190, doi:10.5194/acp-16-6175-2016, 2016.
- 390 Bovensmann, H., Buchwitz, M., Burrows, J. P., Reuter, M., Krings, T., Gerilowski, K., Schneising, O., Hey-
391 mann, J., Tretner, A., and Erzinger, J.: A remote sensing technique for global monitoring of power plant
392 CO₂ emissions from space and related applications, *Atmospheric Measurement Techniques*, 3, 781–811,
393 doi:10.5194/amt-3-781-2010, 2010.
- 394 Brandt, A. R., Heath, G. A., Kort, E. A., O'Sullivan, F., Petron, G., Jordaan, S. M., Tans, P., Wilcox, J.,
395 Gopstein, A. M., Arent, D., Wofsy, S., Brown, N. J., Bradley, R., Stucky, G. D., Eardley, D., and Harriss,
396 R.: Energy and environment. Methane leaks from North American natural gas systems, *Science*, 343, 733–5,
397 doi:10.1126/science.1247045, 2014.
- 398 Brasseur, G. P. and Jacob, D. J.: *Modeling of Atmospheric Chemistry*, Princeton University Press, Princeton,
399 NJ, 2017.
- 400 Buchwitz, M., Reuter, M., Schneising, O., Boesch, H., Guerlet, S., Dils, B., Aben, I., Armante, R., Bergamaschi,
401 P., Blumenstock, T., Bovensmann, H., Brunner, D., Buchmann, B., Burrows, J. P., Butz, A., Chdin, A.,
402 Chevallier, F., Crevoisier, C. D., Deutscher, N. M., Frankenberg, C., Hase, F., Hasekamp, O. P., Heymann,
403 J., Kaminski, T., Laeng, A., Lichtenberg, G., De Mazire, M., Nol, S., Notholt, J., Orphal, J., Popp, C.,
404 Parker, R., Scholze, M., Sussmann, R., Stiller, G. P., Warneke, T., Zehner, C., Bril, A., Crisp, D., Griffith,
405 D. W. T., Kuze, A., O'Dell, C., Oshchepkov, S., Sherlock, V., Suto, H., Wennberg, P., Wunch, D., Yokota,
406 T., and Yoshida, Y.: The Greenhouse Gas Climate Change Initiative (GHG-CCI): Comparison and quality
407 assessment of near-surface-sensitive satellite-derived CO₂ and CH₄ global data sets, *Remote Sensing of*
408 *Environment*, 162, 344–362, doi:10.1016/j.rse.2013.04.024, 2015.
- 409 Buchwitz, M., Schneising, O., Reuter, M., Heymann, J., Krautwurst, S., Bovensmann, H., Burrows, J. P.,
410 Boesch, H., Parker, R. J., Somkuti, P., Detmers, R. G., Hasekamp, O. P., Aben, I., Butz, A., Frankenberg,
411 C., and Turner, A. J.: Satellite-derived methane hotspot emission estimates using a fast data-driven method,

Atmospheric Chemistry and Physics, 17, 5751–5774, doi:10.5194/acp-17-5751-2017, 2017.

Butz, A., Galli, A., Hasekamp, O., Landgraf, J., Tol, P., and Aben, I.: TROPOMI aboard Sentinel-5 Precursor: Prospective performance of CH₄ retrievals for aerosol and cirrus loaded atmospheres, *Remote Sensing of Environment*, 120, 267–276, doi:10.1016/j.rse.2011.05.030, 2012.

Butz, A., Orphal, J., Checa-Garcia, R., Friedl-Vallon, F., von Clarmann, T., Bovensmann, H., Hasekamp, O., Landgraf, J., Knigge, T., Weise, D., Squali-Houssini, O., and Kemper, D.: Geostationary Emission Explorer for Europe (G3E): mission concept and initial performance assessment, *Atmospheric Measurement Techniques*, 8, 4719–4734, doi:10.5194/amt-8-4719-2015, 2015.

Candes, E. J. and Wakin, M. B.: An introduction to compressive sampling, *IEEE Signal Processing Magazine*, 25, 21–30, doi:10.1109/Msp.2007.914731, 2008.

Caulton, D. R., Shepson, P. B., Santoro, R. L., Sparks, J. P., Howarth, R. W., Ingraffea, A. R., Cambaliza, M. O., Sweeney, C., Karion, A., Davis, K. J., Stirm, B. H., Montzka, S. A., and Miller, B. R.: Toward a better understanding and quantification of methane emissions from shale gas development, *Proc Natl Acad Sci U S A*, doi:10.1073/pnas.1316546111, 2014.

Conley, S., Franco, G., Faloon, I., Blake, D. R., Peischl, J., and Ryerson, T. B.: Methane emissions from the 2015 Aliso Canyon blowout in Los Angeles, CA, *Science*, 351, 1317–20, doi:10.1126/science.aaf2348, 2016.

Cressot, C., Chevallier, F., Bousquet, P., Crevoisier, C., Dlugokencky, E. J., Fortems-Cheiney, A., Frankenberg, C., Parker, R., Pison, I., Scheepmaker, R. A., Montzka, S. A., Krummel, P. B., Steele, L. P., and Langenfelds, R. L.: On the consistency between global and regional methane emissions inferred from SCIAMACHY, TANSO-FTS, IASI and surface measurements, *Atmospheric Chemistry and Physics*, 14, 577–592, doi:10.5194/acp-14-577-2014, 2014.

Fishman, J., Iraci, L. T., Al-Saadi, J., Chance, K., Chavez, F., Chin, M., Coble, P., Davis, C., DiGiacomo, P. M., Edwards, D., Eldering, A., Goes, J., Herman, J., Hu, C., Jacob, D. J., Jordan, C., Kawa, S. R., Key, R., Liu, X., Lohrenz, S., Mannino, A., Natraj, V., Neil, D., Neu, J., Newchurch, M., Pickering, K., Salisbury, J., Sosik, H., Subramaniam, A., Tzortziou, M., Wang, J., and Wang, M.: The United States’ Next Generation of Atmospheric Composition and Coastal Ecosystem Measurements: NASA’s Geostationary Coastal and Air Pollution Events (GEO-CAPE) Mission, *Bulletin of the American Meteorological Society*, 93, 1547–1566, doi:10.1175/bams-d-11-00201.1, 2012.

Frankenberg, C., Meirink, J. F., van Weele, M., Platt, U., and Wagner, T.: Assessing methane emissions from global space-borne observations, *Science*, 308, 1010–4, doi:10.1126/science.1106644, 2005.

Frankenberg, C., Thorpe, A. K., Thompson, D. R., Hulley, G., Kort, E. A., Vance, N., Borchardt, J., Krings, T., Gerilowski, K., Sweeney, C., Conley, S., Bue, B. D., Aubrey, A. D., Hook, S., and Green, R. O.: Airborne methane remote measurements reveal heavy-tail flux distribution in Four Corners region, *Proc Natl Acad Sci U S A*, 113, 9734–9, doi:10.1073/pnas.1605617113, 2016.

Fraser, A., Palmer, P. I., Feng, L., Boesch, H., Cogan, A., Parker, R., Dlugokencky, E. J., Fraser, P. J., Krummel, P. B., Langenfelds, R. L., O’Doherty, S., Prinn, R. G., Steele, L. P., van der Schoot, M., and Weiss, R. F.: Estimating regional methane surface fluxes: the relative importance of surface and GOSAT mole fraction measurements, *Atmospheric Chemistry and Physics*, 13, 5697–5713, doi:10.5194/acp-13-5697-2013, 2013.

Houweling, S., Bergamaschi, P., Chevallier, F., Heimann, M., Kaminski, T., Krol, M., Michalak, A. M., and Pa-

tra, P.: Global inverse modeling of CH₄ sources and sinks: An overview of methods, *Atmospheric Chemistry and Physics Discussions*, pp. 1–30, doi:10.5194/acp-2016-572, 2016.

Hu, H., Hasekamp, O., Butz, A., Galli, A., Landgraf, J., Aan de Brugh, J., Borsdorff, T., Scheepmaker, R., and Aben, I.: The operational methane retrieval algorithm for TROPOMI, *Atmospheric Measurement Techniques*, 9, 5423–5440, doi:10.5194/amt-9-5423-2016, 2016.

Hu, H., Landgraf, J., Detmers, R., Borsdorff, T., Aan de Brugh, J., Aben, I., Butz, A., and Hasekamp, O.: Toward Global Mapping of Methane With TROPOMI: First Results and Intersatellite Comparison to GOSAT, *Geophysical Research Letters*, doi:10.1002/2018gl077259, 2018.

Jacob, D. J., Turner, A. J., Maasakkers, J. D., Sheng, J., Sun, K., Liu, X., Chance, K., Aben, I., McKeever, J., and Frankenberg, C.: Satellite observations of atmospheric methane and their value for quantifying methane emissions, *Atmospheric Chemistry and Physics*, 16, 14 371–14 396, doi:10.5194/acp-16-14371-2016, 2016.

Karion, A., Sweeney, C., Ptron, G., Frost, G., Michael Hardesty, R., Kofler, J., Miller, B. R., Newberger, T., Wolter, S., Banta, R., Brewer, A., Dlugokencky, E., Lang, P., Montzka, S. A., Schnell, R., Tans, P., Trainer, M., Zamora, R., and Conley, S.: Methane emissions estimate from airborne measurements over a western United States natural gas field, *Geophysical Research Letters*, 40, 4393–4397, doi:10.1002/grl.50811, 2013.

Karion, A., Sweeney, C., Kort, E. A., Shepson, P. B., Brewer, A., Cambaliza, M., Conley, S. A., Davis, K., Deng, A., Hardesty, M., Herndon, S. C., Lauvaux, T., Lavoie, T., Lyon, D., Newberger, T., Petron, G., Rella, C., Smith, M., Wolter, S., Yacovitch, T. I., and Tans, P.: Aircraft-Based Estimate of Total Methane Emissions from the Barnett Shale Region, *Environ Sci Technol*, 49, 8124–31, doi:10.1021/acs.est.5b00217, 2015.

Kirschke, S., Bousquet, P., Ciais, P., Saunois, M., Canadell, J. G., Dlugokencky, E. J., Bergamaschi, P., Bergmann, D., Blake, D. R., Bruhwiler, L., Cameron-Smith, P., Castaldi, S., Chevallier, F., Feng, L., Fraser, A., Heimann, M., Hodson, E. L., Houweling, S., Josse, B., Fraser, P. J., Krummel, P. B., Lamarque, J.-F., Langenfelds, R. L., Le Qur, C., Naik, V., O'Doherty, S., Palmer, P. I., Pison, I., Plummer, D., Poulter, B., Prinn, R. G., Rigby, M., Ringeval, B., Santini, M., Schmidt, M., Shindell, D. T., Simpson, I. J., Spahni, R., Steele, L. P., Strode, S. A., Sudo, K., Szopa, S., van der Werf, G. R., Voulgarakis, A., van Weele, M., Weiss, R. F., Williams, J. E., and Zeng, G.: Three decades of global methane sources and sinks, *Nature Geoscience*, 6, 813–823, doi:10.1038/ngeo1955, 2013.

Kort, E. A., Frankenberg, C., Costigan, K. R., Lindenmaier, R., Dubey, M. K., and Wunch, D.: Four corners: The largest US methane anomaly viewed from space, *Geophysical Research Letters*, 41, doi:10.1002/2014gl061503, 2014.

Kuze, A., Suto, H., Nakajima, M., and Hamazaki, T.: Thermal and near infrared sensor for carbon observation Fourier-transform spectrometer on the Greenhouse Gases Observing Satellite for greenhouse gases monitoring, *Appl Opt*, 48, 6716–33, doi:10.1364/AO.48.006716, 2009.

Kuze, A., Suto, H., Shiomi, K., Kawakami, S., Tanaka, M., Ueda, Y., Deguchi, A., Yoshida, J., Yamamoto, Y., Kataoka, F., Taylor, T. E., and Buijs, H. L.: Update on GOSAT TANSO-FTS performance, operations, and data products after more than 6 years in space, *Atmospheric Measurement Techniques*, 9, 2445–2461, doi:10.5194/amt-9-2445-2016, 2016.

Lavoie, T. N., Shepson, P. B., Cambaliza, M. O., Stirm, B. H., Karion, A., Sweeney, C., Yacovitch, T. I., Herndon, S. C., Lan, X., and Lyon, D.: Aircraft-Based Measurements of Point Source Methane Emissions in the Barnett Shale Basin, *Environ Sci Technol*, 49, 7904–13, doi:10.1021/acs.est.5b00410, 2015.

492 Lin, J. C., Gerbig, C., Wofsy, S. C., Andrews, A. E., Daube, B. C., Davis, K. J., and Grainger, C. A.: A near-
 493 field tool for simulating the upstream influence of atmospheric observations: The Stochastic Time-Inverted
 494 Lagrangian Transport (STILT) model, *Journal of Geophysical Research-Atmospheres*, 108, ACH 2–1–ACH
 495 2–17, doi:10.1029/2002jd003161, 2003.

496 Lyon, D. R., Zavala-Araiza, D., Alvarez, R. A., Harriss, R., Palacios, V., Lan, X., Talbot, R., Lavoie, T.,
 497 Shepson, P., Yacovitch, T. I., Herndon, S. C., Marchese, A. J., Zimmerle, D., Robinson, A. L., and Hamburg,
 498 S. P.: Constructing a Spatially Resolved Methane Emission Inventory for the Barnett Shale Region, *Environ*
 499 *Sci Technol*, 49, 8147–57, doi:10.1021/es506359c, 2015.

500 Maasakkers, J. D., Jacob, D. J., Sulprizio, M. P., Turner, A. J., Weitz, M., Wirth, T., Hight, C., DeFigueiredo,
 501 M., Desai, M., Schmeltz, R., Hockstad, L., Bloom, A. A., Bowman, K. W., Jeong, S., and Fischer, M. L.:
 502 Gridded National Inventory of U.S. Methane Emissions, *Environ Sci Technol*, 50, 13 123–13 133, doi:10.
 503 1021/acs.est.6b02878, 2016.

504 Miller, S. M., Wofsy, S. C., Michalak, A. M., Kort, E. A., Andrews, A. E., Biraud, S. C., Dlugokencky,
 505 E. J., Eluszkiewicz, J., Fischer, M. L., Janssens-Maenhout, G., Miller, B. R., Miller, J. B., Montzka, S. A.,
 506 Nehrkorn, T., and Sweeney, C.: Anthropogenic emissions of methane in the United States, *Proc Natl Acad*
 507 *Sci U S A*, 110, 20018–22, doi:10.1073/pnas.1314392110, 2013.

508 Monteil, G., Houweling, S., Butz, A., Guerlet, S., Schepers, D., Hasekamp, O., Frankenberg, C., Scheep-
 509 maker, R., Aben, I., and Rckmann, T.: Comparison of CH₄ inversions based on 15 months of GOSAT
 510 and SCIAMACHY observations, *Journal of Geophysical Research: Atmospheres*, 118, 11,807–11,823, doi:
 511 10.1002/2013jd019760, 2013.

512 O’Brien, D. M., Polonsky, I. N., Utembe, S. R., and Rayner, P. J.: Potential of a geostationary geoCARB
 513 mission to estimate surface emissions of CO₂, CH₄ and CO in a polluted urban environment: case study
 514 Shanghai, *Atmospheric Measurement Techniques*, 9, 4633–4654, doi:10.5194/amt-9-4633-2016, 2016.

515 O’Dell, C. W., Connor, B., Bsch, H., O’Brien, D., Frankenberg, C., Castano, R., Christi, M., Eldering, D.,
 516 Fisher, B., Gunson, M., McDuffie, J., Miller, C. E., Natraj, V., Oyafuso, F., Polonsky, I., Smyth, M., Taylor,
 517 T., Toon, G. C., Wennberg, P. O., and Wunch, D.: The ACOS CO₂ retrieval algorithm Part 1: Description
 518 and validation against synthetic observations, *Atmospheric Measurement Techniques*, 5, 99–121, doi:10.
 519 5194/amt-5-99-2012, 2012.

520 Peischl, J., Ryerson, T. B., Aikin, K. C., de Gouw, J. A., Gilman, J. B., Holloway, J. S., Lerner, B. M., Nadkarni,
 521 R., Neuman, J. A., Nowak, J. B., Trainer, M., Warneke, C., and Parrish, D. D.: Quantifying atmospheric
 522 methane emissions from the Haynesville, Fayetteville, and northeastern Marcellus shale gas production re-
 523 gions, *Journal of Geophysical Research-Atmospheres*, 120, 2119–2139, doi:10.1002/2014JD022697, 2015.

524 Peischl, J., Karion, A., Sweeney, C., Kort, E. A., Smith, M. L., Brandt, A. R., Yeskoo, T., Aikin, K. C., Conley,
 525 S. A., Gvakharia, A., Trainer, M., Wolter, S., and Ryerson, T. B.: Quantifying atmospheric methane emis-
 526 sions from oil and natural gas production in the Bakken shale region of North Dakota, *Journal of Geophysical*
 527 *Research: Atmospheres*, 121, 6101–6111, doi:10.1002/2015jd024631, 2016.

528 Polonsky, I. N., O’Brien, D. M., Kumer, J. B., and O’Dell, C. W.: Performance of a geostationary mission, geo-
 529 CARB, to measure CO₂, CH₄ and CO column-averaged concentrations, *Atmospheric Measurement Tech-*
 530 *niques*, 7, 959–981, doi:10.5194/amt-7-959-2014, 2014.

531 Rayner, P. J., Utembe, S. R., and Crowell, S.: Constraining regional greenhouse gas emissions using geostation-

ary concentration measurements: a theoretical study, *Atmospheric Measurement Techniques*, 7, 3285–3293, doi:10.5194/amt-7-3285-2014, 2014.

Rodgers, C. D.: *Inverse Methods for Atmospheric Sounding*, World Scientific, Singapore, 2000.

Saunois, M., Bousquet, P., Poulter, B., Peregon, A., Ciais, P., Canadell, J. G., Dlugokencky, E. J., Etiope, G., Bastviken, D., Houweling, S., Janssens-Maenhout, G., Tubiello, F. N., Castaldi, S., Jackson, R. B., Alexe, M., Arora, V. K., Beerling, D. J., Bergamaschi, P., Blake, D. R., Brailsford, G., Brovkin, V., Bruhwiler, L., Crevoisier, C., Crill, P., Covey, K., Curry, C., Frankenberg, C., Gedney, N., Hglund-Isaksson, L., Ishizawa, M., Ito, A., Joos, F., Kim, H.-S., Kleinen, T., Krummel, P., Lamarque, J.-F., Langenfelds, R., Locatelli, R., Machida, T., Maksyutov, S., McDonald, K. C., Marshall, J., Melton, J. R., Morino, I., Naik, V., and Peters, G. P.: The global methane budget 2000–2012, *Earth System Science Data*, 8, 697–751, doi:10.5194/essd-8-697-2016, 2016.

Sheng, J.-X., Jacob, D. J., Turner, A. J., Maasakkers, J. D., Benmergui, J., Bloom, A. A., Arndt, C., Gautam, R., Zavala-Araiza, D., Boesch, H., and Parker, R. J.: 2010–2015 methane trends over Canada, the United States, and Mexico observed by the GOSAT satellite: contributions from different source sectors, *Atmospheric Chemistry and Physics Discussions*, pp. 1–18, doi:10.5194/acp-2017-1110, 2018a.

Sheng, J.-X., Jacob, D. J., Turner, A. J., Maasakkers, J. D., Sulprizio, M. P., Bloom, A. A., Andrews, A. E., and Wunch, D.: High-resolution inversion of methane emissions in the Southeast US using SEAC⁴RS aircraft observations of atmospheric methane: anthropogenic and wetland sources, *Atmospheric Chemistry and Physics Discussions*, pp. 1–17, doi:10.5194/acp-2017-1151, 2018b.

Skamarock, W. C., Klemp, J. B., Dudhia, J., Gill, D. O., Barker, D. M., Duda, M. G., Huang, X.-Y., Wang, W., and Powers, J. G.: A Description of the Advanced Research WRF Version 3, Tech. rep., National Center for Atmospheric Research, doi:10.5065/D68S4MVH, 2008.

Tan, Z., Zhuang, Q., Henze, D. K., Frankenberg, C., Dlugokencky, E., Sweeney, C., Turner, A. J., Sasakawa, M., and Machida, T.: Inverse modeling of pan-Arctic methane emissions at high spatial resolution: what can we learn from assimilating satellite retrievals and using different process-based wetland and lake biogeochemical models?, *Atmospheric Chemistry and Physics*, 16, 12 649–12 666, doi:10.5194/acp-16-12649-2016, 2016.

Tarantola, A.: *Inverse Problem Theory and Methods for Model Parameter Estimation*, Society for Industrial and Applied Mathematics, Philadelphia, PA, USA, 2004.

Turner, A. J. and Jacob, D. J.: Balancing aggregation and smoothing errors in inverse models, *Atmospheric Chemistry and Physics*, 15, 7039–7048, doi:10.5194/acp-15-7039-2015, 2015.

Turner, A. J., Jacob, D. J., Wecht, K. J., Maasakkers, J. D., Lundgren, E., Andrews, A. E., Biraud, S. C., Boesch, H., Bowman, K. W., Deutscher, N. M., Dubey, M. K., Griffith, D. W. T., Hase, F., Kuze, A., Notholt, J., Ohyama, H., Parker, R., Payne, V. H., Sussmann, R., Sweeney, C., Velasco, V. A., Warneke, T., Wennberg, P. O., and Wunch, D.: Estimating global and North American methane emissions with high spatial resolution using GOSAT satellite data, *Atmospheric Chemistry and Physics*, 15, 7049–7069, doi:10.5194/acp-15-7049-2015, 2015.

572 Turner, A. J., Jacob, D. J., Benmergui, J., Wofsy, S. C., Maasakkers, J. D., Butz, A., Hasekamp, O., and Biraud,
 573 S. C.: A large increase in U.S. methane emissions over the past decade inferred from satellite data and surface
 574 observations, *Geophysical Research Letters*, pp. 2218–2224, doi:10.1002/2016gl067987, 2016a.

575 Turner, A. J., Shusterman, A. A., McDonald, B. C., Teige, V., Harley, R. A., and Cohen, R. C.: Network
 576 design for quantifying urban CO₂ emissions: assessing trade-offs between precision and network density,
 577 *Atmospheric Chemistry and Physics*, 16, 13 465–13 475, doi:10.5194/acp-16-13465-2016, 2016b.

578 Turner, A. J., Frankenberg, C., Wennberg, P. O., and Jacob, D. J.: Ambiguity in the causes for decadal trends
 579 in atmospheric methane and hydroxyl, *Proc Natl Acad Sci U S A*, 114, 5367–5372, doi:10.1073/pnas.
 580 1616020114, 2017.

581 Veefkind, J. P., Aben, I., McMullan, K., Frster, H., de Vries, J., Otter, G., Claas, J., Eskes, H. J., de Haan, J. F.,
 582 Kleipool, Q., van Weele, M., Hasekamp, O., Hoogeveen, R., Landgraf, J., Snel, R., Tol, P., Ingmann, P.,
 583 Voors, R., Kruizinga, B., Vink, R., Visser, H., and Levelt, P. F.: TROPOMI on the ESA Sentinel-5 Precursor:
 584 A GMES mission for global observations of the atmospheric composition for climate, air quality and ozone
 585 layer applications, *Remote Sensing of Environment*, 120, 70–83, doi:10.1016/j.rse.2011.09.027, 2012.

586 Wecht, K. J., Jacob, D. J., Frankenberg, C., Jiang, Z., and Blake, D. R.: Mapping of North American methane
 587 emissions with high spatial resolution by inversion of SCIAMACHY satellite data, *Journal of Geophysical
 588 Research: Atmospheres*, 119, 7741–7756, doi:10.1002/2014jd021551, 2014a.

589 Wecht, K. J., Jacob, D. J., Sulprizio, M. P., Santoni, G. W., Wofsy, S. C., Parker, R., Bsch, H., and Worden, J.:
 590 Spatially resolving methane emissions in California: constraints from the CalNex aircraft campaign and from
 591 present (GOSAT, TES) and future (TROPOMI, geostationary) satellite observations, *Atmospheric Chemistry
 592 and Physics*, 14, 8173–8184, doi:10.5194/acp-14-8173-2014, 2014b.

593 Worden, J. R., Turner, A. J., Bloom, A., Kulawik, S. S., Liu, J., Lee, M., Weidner, R., Bowman, K., Frankenberg,
 594 C., Parker, R., and Payne, V. H.: Quantifying lower tropospheric methane concentrations using GOSAT
 595 near-IR and TES thermal IR measurements, *Atmospheric Measurement Techniques*, 8, 3433–3445, doi:
 596 10.5194/amt-8-3433-2015, 2015.

597 Xi, X., Natraj, V., Shia, R. L., Luo, M., Zhang, Q., Newman, S., Sander, S. P., and Yung, Y. L.: Simulated
 598 retrievals for the remote sensing of CO₂, CH₄, CO, and H₂O from geostationary orbit, *Atmospheric Mea-
 599 surement Techniques*, 8, 4817–4830, doi:10.5194/amt-8-4817-2015, 2015.

600 Zavala-Araiza, D., Lyon, D. R., Alvarez, R. A., Davis, K. J., Harriss, R., Herndon, S. C., Karion, A., Kort,
 601 E. A., Lamb, B. K., Lan, X., Marchese, A. J., Pacala, S. W., Robinson, A. L., Shepson, P. B., Sweeney,
 602 C., Talbot, R., Townsend-Small, A., Yacovitch, T. I., Zimmerle, D. J., and Hamburg, S. P.: Reconciling
 603 divergent estimates of oil and gas methane emissions, *Proc Natl Acad Sci U S A*, 112, 15 597–602, doi:
 604 10.1073/pnas.1522126112, 2015.